The key role of very-low-energy-electrons in tin-based molecular resists for extreme ultraviolet nanolithography

Bespalov, I.; Zhang, Y.; Haitjema, J.; Tromp, R.M.; Molen, S.J. van der; Brouwer, A.M.; ... ; Castellanos, S.

ACS APPLIED MATERIALS & INTERFACES

www.acsami.org

Research Article

Key Role of Very Low Energy Electrons in Tin-Based Molecular Resists for Extreme Ultraviolet Nanolithography

Ivan Bespalov,* Yu Zhang, Jarich Haitjema, Rudolf M. Tromp, Sense Jan van der Molen, Albert M. Brouwer, Johannes Jobst,* and Sonia Castellanos*

Cite This: https://dx.doi.org/10.1021/acsami.9b19004

Read Online

ACCESS | Metrics & More | Article Recommendations | Supporting Information

ABSTRACT: Extreme ultraviolet (EUV) lithography (13.5 nm) is the newest technology that allows high-throughput fabrication of electronic circuitry in the sub-20 nm scale. It is commonly assumed that low-energy electrons (LEEs) generated in the resist materials by EUV photons are mostly responsible for the solubility switch that leads to nanopattern formation. Yet, reliable quantitative information on this electron-induced process is scarce. In this work, we combine LEE microscopy (LEEM), electron energy loss spectroscopy (EELS), and atomic force microscopy (AFM) to study changes induced by electrons in the 0−40 eV range in thin films of a state-of-the-art molecular organometallic EUV resist known as tin-oxo cage. LEEM−EELS uniquely allows to correct for surface charging and thus to accurately determine the electron landing energy. AFM postexposure analyses revealed that irradiation of the resist with LEEs leads to the densification of the resist layer because of carbon loss. Remarkably, electrons with energies as low as 1.2 eV can induce chemical reactions in the Sn-based resist. Electrons with higher energies are expected to cause electronic excitation or ionization, opening up more pathways to enhanced conversion. However, we do not observe a substantial increase of chemical conversion (densification) with the electron energy increase in the 2−40 eV range. Based on the dose-dependent thickness profiles, a simplified reaction model is proposed where the resist undergoes sequential chemical reactions, first yielding a sparsely cross-linked network and then a more densely cross-linked network. This model allows us to estimate a maximum reaction volume on the initial material of 0.15 nm^3 per incident electron in the energy range studied, which means that about 10 LEEs per molecule on average are needed to turn the material insoluble and thus render a pattern. Our observations are consistent with the observed EUV sensitivity of tin-oxo cages.

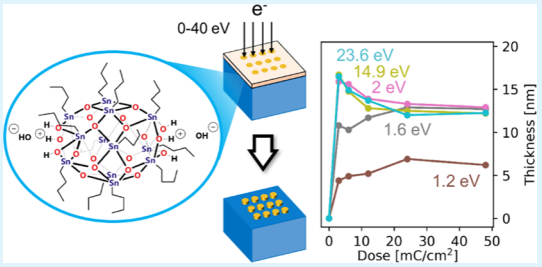

KEYWORDS: *low-energy electron microscopy, electron energy loss spectroscopy, patterning, electron-induced chemistry, inorganic EUV resist*

INTRODUCTION

As the miniaturization of electronic components in computer chips continues, novel nanopatterning technologies are necessary to attain a cost-effective high-volume manufacturing.[1] Among all nanopatterning approaches, extreme ultraviolet lithography (EUVL) is the most promising candidate to reach the targeted sub-20 nm resolution by employing a much shorter wavelength (13.5 nm) than it is used in current deep UV (DUV) lithography (193 nm).[2] One of the biggest challenges in the establishment of EUVL in the semiconductor industry lies in the interaction of the high-energy (92 eV) EUV radiation with the photoresist material. Conventional polymer-based photoresists designed for DUV lithography offer relatively low EUV photon absorption, which limits their performance.[3] Therefore, the search for new materials that can absorb an optimal amount of EUV light and render high-quality nanopatterns is essential for EUVL technology.[4−6]

Among the variety of materials that are being investigated for EUVL applications, metal−organic materials, also called inorganic resists, are considered the most promising. Their main advantage is that the incorporation of metallic elements enhances EUV absorptivity.[7] In particular, Sn-containing materials have attracted much attention as they can yield nanopatterns at relatively low doses.[8−10] Yet, a lack of detailed understanding of the chemical processes occurring upon the absorption of EUV photons hinders the rational design of efficient resists. When an EUV photon is absorbed by the resist, primary and secondary electrons (SEs) with energies in the 0−80 eV range are produced.[11,12] These electrons play a central role in the chemical transformations that photoresists undergo. Specifically, they can induce molecular bond scissions,[13,14] which change the photoresist structure and thus its solubility properties, thereby enabling pattern formation.[11,15−21] However, very few studies of the electron

Received: October 21, 2019
Accepted: February 5, 2020
Published: February 5, 2020

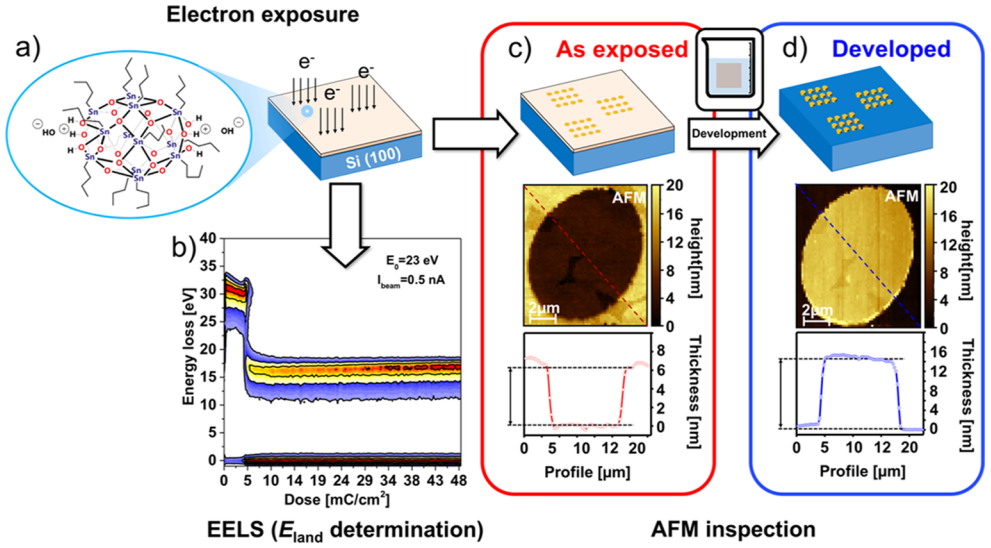

Figure 1. (a) Chemical structure of the tin-oxo cage compound with hydroxide counterions (TinOH). (b) Example of a transient EELS spectrum during electron exposure. (c,d) Inspection by AFM of electron-induced changes in a thin film (20 nm) of TinOH exposed to electrons of E_{land} = 15.8 eV and an exposure dose of 12 mC/cm^2 in LEEM. (c) The exposed area is clearly visible in the AFM image on the "as-exposed" film before development. The difference in thickness between exposed and unexposed areas is shown below in the profile line scan along the red dashed line. (d) AFM image of the same area shown in (c) after development. The thickness of the insoluble material left after development is shown below as a height profile line scan along the blue dashed line.

energy dependence of these processes have been performed up to date.[15,17,22−24]

Gaining knowledge on which electrons induce more significant changes in EUV photoresists is of high relevance both from a fundamental and an applied point of view. Mainly, the efficiency of electron-induced reactions contributes to the overall sensitivity of the photoresists.[18,19] At the same time, the so-called electron blur in the final nanopattern—the maximum distance away from the photon absorption point where electrons induce solubility changes—depends on the electron mean free path.[25] Accurate experimental values for the mean free paths of electrons below 100 eV are scarce, and only recently, it has been experimentally shown that they strongly depend on electron energy and on the material.[26] Understanding interactions of low-energy electrons (LEEs) with photoresist materials and the energy dependence of those interactions thus presents an essential contribution to estimate, and eventually control, the efficiency of the photoresist as well as their lateral blur in the nanopatterns.

In the present work, we use LEE microscopy (LEEM) to expose thin films of a Sn-based EUV resist with LEEs within the 0−40 eV energy range, which is representative of the SE generated upon EUVL. We use electron energy loss spectroscopy (EELS) to determine with accuracy the energies of the electrons that impinge the photoresist, correcting for surface charging effects that result from the poorly conducting character of the material. Next, using atomic force microscopy (AFM), we study the electron-induced structural changes as a function of electron energy and exposure dose and relate them to the changes in the solubility properties of the material. These experiments allow us to estimate the average reaction volume per incident electron as a function of electron energy. Similarly, we estimate a "chemical efficiency" of LEEs in the 0−40 eV range in terms of number of electrons needed per molecule to render the material insoluble.

RESULTS AND DISCUSSION

We study films of tin-oxo cages, a molecular material referred to as TinOH, where OH stands for the two hydroxyl counterions[27,28] (Figure 1a). This compound is a Sn-containing material that has proven to be a promising EUV resist.[8,10,29,30] The mechanism responsible for the solubility change of TinOH promoted by EUV photons was proposed in previous works.[8−10,31] Here, we investigate how LEEs directly induce changes in the solubility properties of this material as a function of electron energy and dose within a relevant energy window for EUVL (0−40 eV).[15,32−34] The design of our LEEM experimental setup allows us to evaluate the effect of LEEs on the photoresist using in situ and ex situ approaches. In the in situ approach, the interaction of LEEs with the photoresist is monitored using LEEM-based EELS (Figure 1b). The ex situ approach consists of exposure to LEEs, followed by AFM analysis both before and after a development step is applied to the resist layer (Figure 1c,d).

In Situ EELS Experiments: Surface Charging. When a poorly conducting resist layer is exposed to LEEs, the resulting surface charging can severely affect the electron/resist interaction energy. This phenomenon has been studied in thin films of polymethyl methacrylate (PMMA)[35] and is crucial for an accurate understanding of the electron exposure experiments. To quantify the dynamic charging effects in the present experiment, EELS spectra were recorded during the electron exposure of different primary electron beam energies (E_0) in the 0−40 eV range. E_0 is defined as the potential difference between the electron gun (−15 keV) and the potential applied to the sample (V_s), corrected by the work function difference $\Delta\Phi$ between the electron emitter and the sample (E_0 = −15 keV + eV_s + $\Delta\Phi$). In ref 36, we have shown that the width of the EELS spectrum, that is, the difference between the zero-loss peak and the SE cutoff, provides a direct measurement of the electron landing energy (E_{land}), that is, the actual energy that the electrons have when they reach the surface of the sample. Given that TinOH is a poorly

https://dx.doi.org/10.1021/acsami.9b19004
ACS Appl. Mater. Interfaces XXXX, XXX, XXX−XXX

conducting material, E_{land} is in general not equal to E_0 because of charging effects. Hence, we use the width of the EELS spectrum during exposure (Figure 1b) in these experiments to determine E_{land}, the true interaction energy.

To do so, for each particular setting of E_0, the time evolution of the EELS spectrum was recorded during electron exposure up to a dose of 56 mC/cm^2. Examples of such measurements are shown in Figures 1b and 2a–c, which display the energy

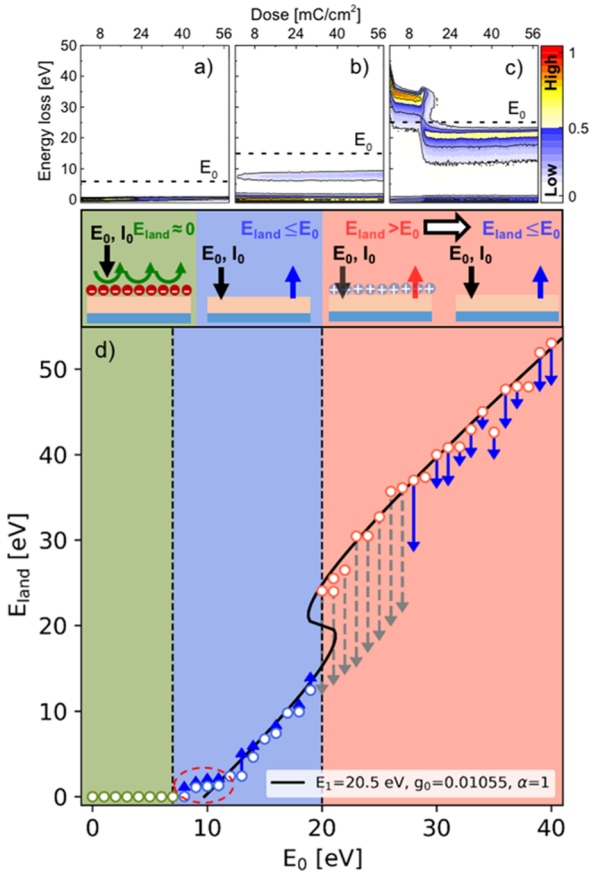

Figure 2. Effect of photoresist surface charging during electron exposure on E_{land} measured by LEEM-EELS. (a–c) EELS spectra recorded during the exposure of 20 nm thick TinOH films to E_0 = 7 (a), 16 (b), and 26 eV (c). (d) Dependence of the measured E_{land} on E_0 (I_0 = 0.017 nA/μm^2). White-filled circles represent the E_{land} values at dose = 0 in (a–c). The solid line plots the fit of the experimental result using the cusp catastrophe equation developed in ref 35 for normalized conductance, g_0 = 0.01055, and E_1 = 20.5 eV, where E_1 is the energy at which SE emission equals the incident electron flux. The arrows indicate the evolution of E_{land} with increasing dose at each E_0: blue arrows for gradual shifts and dashed arrows for abrupt drops of E_{land} as the SE emission coefficient switches from >1 to <1. The dashed red ellipse highlights the E_0 energies where E_{land} fluctuates around zero.

distribution of the electrons reflected and emitted by the sample as a function of exposure dose at a constant value of E_0. The y-axis thus corresponds to an energy-"loss" scale—the width of the EELS spectra that gives E_{land}—, and the x-axis to the dose, which is proportional to the exposure time, that is, dose = time × current density (Figures 1b and 2a–c).

In Figure 2, it can be observed that three surface charging regimes can be distinguished in three different ranges of E_0. In the green area of Figure 2d (E_0 = 0–7 eV, E_{land} ≈ 0), the photoresist surface is charged negatively[37] and repels all incident electrons so that only the zero-loss peak is observed in the EELS spectrum (Figure 2a). In the blue area (E_0 = 7–19 eV, 0 < E_{land} < E_0 < E_1 = 20 eV), the negative charge decreases because of increasing SE emission, and incoming electrons interact with the sample with energy E_{land}. In the red area (E_{land} > E_0 > E_1 = 20 eV), SE emission coefficient is greater than unity and surface charging is positive. As a consequence, E_{land} is higher than E_0. Chemical changes on the sample induced by the electrons lead to a decrease of the secondary emission coefficient (i.e., increase in E_1) over time (dose) as well as to a slight increase in the normalized conductance (g_0) of the film (see Figure S1 in the Supporting Information). This induces a shift in E_{land} during exposure, which is represented by arrows in Figure 2d. The increase of E_1 with exposure leads to a shift of the blue/red boundary to higher values of E_0, and a decrease of the SE emission coefficient leads to a value below 1 after a certain dose, which is accompanied by a sudden drop from E_{land} > E_0 > E_1 to E_{land} < E_0 < E_1 (Figure 2c), represented with the dashed arrows in Figure 2d. These observations are in agreement with previous results on PMMA and can be quantitatively described by a so-called catastrophe theory.[35] The black S-shaped curve in Figure 2d is a fit to the zero-exposure data based on this theory. More details about the theory and the evolution of the S-curve with electron exposure dose can be found in ref 35.

In the rest of this work, we will use the measured E_{land} values (Figure 2d) to define the energy of the incident electrons.

Ex Situ AFM Analysis: Electron-Induced Densification and Solubility Changes. Postexposure AFM inspection was used to monitor changes in the resist film thickness induced by electrons of different energies and at different doses, as well as for detecting changes in the solubility properties of the resist. For the latter purpose, the sample was immersed in a developer (2-heptanone/water mixture) that selectively dissolves the starting material but not the products formed upon exposure.[15] Examples of AFM images recorded before ("as-exposed") and after development ("developed") are shown in Figure 1c,d, respectively. In the "as-exposed" sample (Figure 1c), the dark ellipse reveals that the irradiated area undergoes a substantial thickness decrease (densification) with respect to the surrounding nonirradiated area. After development, the unexposed resist is washed away, leaving behind only the exposed areas that have turned insoluble because of electron-induced chemistry (Figure 1d). To quantify the densification and the amount of the insoluble material, the film thickness of the same exposed areas is measured before and after development by means of AFM and is plotted as a function of electron energy and dose in Figure 3.

The thickness of the exposed areas ("as-exposed") significantly decreases with increasing electron dose and energy (Figure 3a,b). Given the low electron energy and current density, we dismiss beam-induced, direct evaporation of whole molecules as the origin of thickness loss and attribute it to a densification of the resist layer as a result of electron-induced chemical reactions. Such a densification has also been observed in layers of this material upon EUV exposure when they are exposed beyond the dose that renders the whole thin film insoluble.[29]

At each given dose, the film thickness decreases to the same value for all electrons with E_{land} > 2 eV (Figure 3a), which indicates that the densification induced by electrons in the 4–36 eV range is rather similar. Yet, the densification increases with the dose, reaching a maximum value at the highest dose

https://dx.doi.org/10.1021/acsami.9b19004
ACS Appl. Mater. Interfaces XXXX, XXX, XXX–XXX

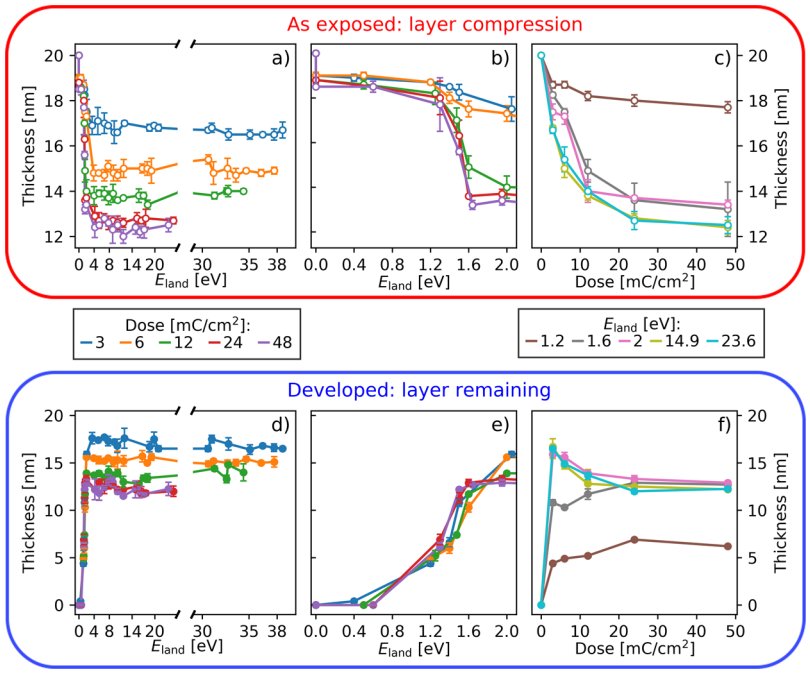

Figure 3. Thickness measured on a 20 nm thick TinOH resist layer exposed to LEEs (I_0 = 0.017 nA/μm^2) as a function of electron energy (E_{land}) before development, i.e., displaying the layer compression (a) and zoomed-in plot (b); after development, i.e., displaying the thickness of the insoluble layer that remains (d) and zoomed-in plot (e); and as a function of dose for some selected energies before (c) and after (f) development.

used in our experiments, 48 mC/cm^2. The evolution of densification is even clearer when thickness is plotted as a function of dose at a given E_{land} (Figure 3c). It appears that electrons of 0−1.4 eV in the measured dose range do not yield as much densification. Yet, it should be noticed that in the onset region where E_{land} starts to deviate from zero (red dashed circle in Figure 2d), relatively small (10−20%) fluctuations in the incident electron current during electron exposure will have the effect of E_{land} fluctuating around zero. Therefore, only a fraction of the incident electrons impinges on the sample and the actual dose on the material is lower than intended. Thus, the resist reactivity appears to be reduced. Unfortunately, it is not possible at present to measure the exact dose reduction in this narrow energy window. For E_{land} > ∼2 eV, this effect no longer occurs, and the exposure dose is unambiguous.

The thickness evolution due to electron exposure observed in the "as-exposed" films (Figure 3a,b) is mirrored in its "developed" version (Figure 3c,d). During development, the unexposed material is washed away, whereas the material in the irradiated areas remains, in line with the negative tone behavior previously reported for this resist.[10,29,30] This shows that the chemical changes that lead to thickness shrinking are also responsible for changes in the solubility of the material. As for the "as-exposed" sample, for E_{land} > 2, the remaining thickness after development (Figure 3c) does not vary significantly with the energy increase for a given dose. However, the layer thickness decreases with increasing doses, reflecting the densification trends already observed in the undeveloped material.

In Figure 3d, the plots of the remaining "developed" thickness as a function of dose resemble the contrast curves commonly used in photolithography to evaluate resists sensitivity.[29] There, the minimum dose of light of a specific wavelength necessary to induce a solubility switch (from soluble to insoluble in the case of a negative tone resist) can be determined from the onset of the curve. In the present curves, the dose onset is below 3 mC/cm^2 in all cases. Importantly, even very LEEs (1.2 eV electrons) can already induce chemical reactions that yield changes in the solubility properties of the material.

For all curves resulting from exposure to electrons with E_{land} ≥ 2 eV, a maximum thickness value is reached at the lowest dose (3 mC/cm^2) before decreasing to an almost constant value for doses above 24 mC/cm^2. Such a profile indicates that at low doses, an insoluble product with a relatively low degree of densification is formed, which keeps reacting and densifying as the electron dose is increased. It is known that exposure of TinOH to DUV photons leads to Sn−C bond cleavage, which yields volatile products derived from butyl chains that outgas from the film.[8] Also, butyl fragments have been detected in electron-induced desorption experiments performed on similar Sn oxo cages with 80 eV electrons.[38] Because the butyl chains represent up to a ∼70% of the molecule volume[27] (see Figure S3 in the Supporting Information), the cleavage of butyl chains necessarily renders a significant decrease of film thickness. As a reference, a complete transformation of the TinOH film (density in the crystalline form 1.84 g/cm^3, giving a molar volume of 1341.6 cm^3/mol) to pure SnO_2 (density in the crystalline form 6.95 g/cm^3, giving a molar volume of 38.8 cm^3/mol) would lead to a compaction of ∼65%, that is, from 20 to 7 nm. Hence, we attribute the observed "as-exposed" densification to carbon-loss reactions. In addition, for similar Sn-based materials, it has been proposed that the Sn−C bond cleavage yields active Sn sites prone to form bonds with neighboring activated sites. This leads to the subsequent aggregation of the inorganic clusters and the creation of an insoluble network.[21] Given that TinOH has 12 carbon chains per molecule, we expect a gradual butyl cleavage and cross-linking of the inorganic residues with increasing EUV or LEE irradiation, resulting in an increasingly denser material. In addition, other reactions involving Sn−O bond cleavage might

https://dx.doi.org/10.1021/acsami.9b19004
ACS Appl. Mater. Interfaces XXXX, XXX, XXX−XXX

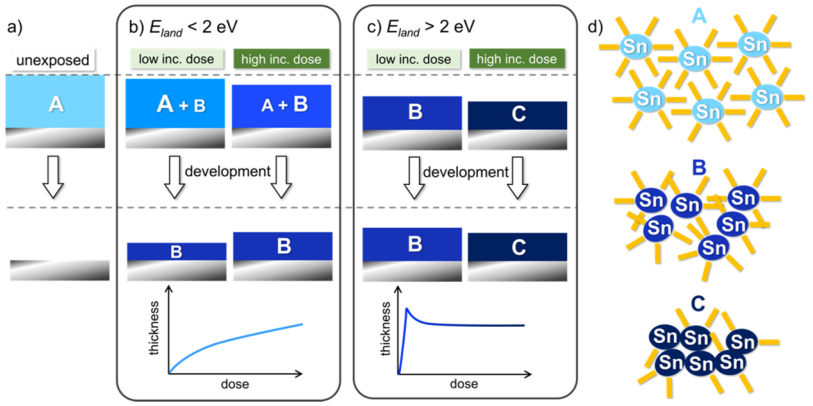

Figure 4. Scheme representing the densification of the TinOH material **A**. (a) Unexposed resist is removed completely during the development. (b) For electron exposure with E_{land} < 2 eV, only a small fraction of electrons impinging on the surface reach the material and only low conversion is attained. (c) For E_{land} > 2 eV, as the incident (inc.) dose increases, consecutive reactions yield the insoluble products **B** (denser than **A**) and **C** (denser than **B**). (d) Schematic representation of the initial TinOH molecular material **A** and of the two insoluble networks **B** and **C**. Blue ellipses represent the Sn-based inorganic core and orange bars the butyl chains.

also occur to a certain extent, which would also have an impact on the densification of the material.

In order to relate the thickness curves in Figure 3 to chemical changes, we simplify this complex process of reactions in a model where two types of products (materials **B** and **C**) with different densities are formed in sequence from the original TinOH (material **A**), that is, through consecutive reactions **A** → **B** → **C**.

As schematically shown in Figure 4, upon electron exposure, the initial resist material **A** transforms first into an insoluble product **B** with higher density than **A** because of few butyl-chain cleavage events, loss of the carbon chain by desorption, and cross-linking among the few molecular units through the "activated" Sn sites (the ones that underwent Sn−C bond cleavage). Product **B** thus represents the mixture of relatively low-weight oligomers that are cross-linked to a low degree. The **A** → **B** reaction requires low doses and the subsequent electrons can promote further carbon loss and aggregation of the inorganic units, leading to the **B** → **C** evolution, where **C** has an even denser structure (Figure 4b). Product **C** in this model thus represents a network with a high degree of cross-linking among the Sn-containing core units and with a low carbon content. This transformation of the material with the dose results in a 9% increase of the material conductance (g_0) deduced from the fitting of the S-curves that result from surface charging evolution charging over dose (see Figure S1 in the Supporting Information).

For very LEEs (1.2 and 1.6 eV), the number of electrons that reach the resist at the given incident doses is not sufficient to transform all initial material **A** to the insoluble **B** or **C** and a mixture of mainly **A** + **B** is formed in the exposed areas. This is the same behavior observed in photoresists when the photon dose applied is not sufficient for a full conversion of the initial material into insoluble material.[39,40] In this underexposed regime, the thickness of the exposed film is reduced in the development step because the remaining material **A** is dissolved (Figure 4a).

The fraction of unreacted material **A** left in the exposed areas can thus be calculated by comparing the thickness of the film after compression (cf. "as exposed" in Figure 3c), which is a mixture of **A** and **B**, and the thickness remaining after development (cf. "developed" in Figure 3f), which consists only of the insoluble material (**B** at lower doses and **C** at higher doses). Figure 5a shows the thickness lost during development as a function of exposure dose for some selected

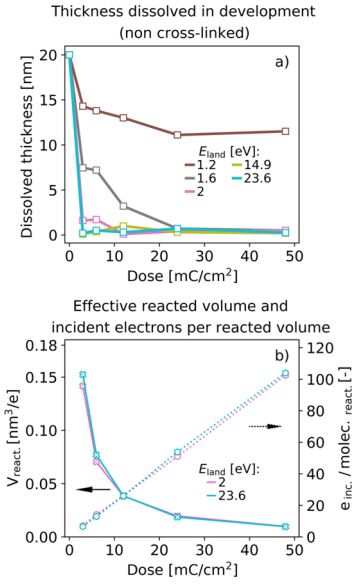

Figure 5. (a) Thickness of starting material **A** (noncross-linked TinOH) dissolved in the development step for each dose of electrons of different energies (E_{land}). (b) Effective reacted volume per impinging electron (continuous line) and the number of incident electrons per reacted molecule (dashed lines) estimated for every exposure dose to electrons of selected energies.

electron energies. It thus plots the conversion of the starting material **A** as a function of electron dose for the different energies. It can be observed that a 3 mC/cm^2 dose of electrons with an energy of 2 eV is already sufficient to transform the layer of the initial material into the insoluble mixture that we identify as **B**. This dose, corresponding to an energy dose of 9 mJ/cm^2, is in the range of dose needed to transform the whole thickness of the material (D_{100}) when using EUV light: for a 40 nm film, ca. 50 mJ/cm^2 of EUV incident dose are required,[29] from which 38% is absorbed,[41] that is, ca. 19 mJ/cm^2.

A likely mechanism leading to carbon-chain loss in TinOH is electron capture, followed by the decomposition of the radical anion formed. This process, known as dissociative electron

https://dx.doi.org/10.1021/acsami.9b19004
ACS Appl. Mater. Interfaces XXXX, XXX, XXX−XXX

attachment, can be promoted by electrons of very low kinetic energies of the added electron, sometimes even 0 eV,[13,14,42−44] and is likely to occur in metal−carbon bonds[42−44] like Sn−C[38] in TinOH. Molecular quantum chemical calculations (see the Supporting Information) support the notion that the radical anion formed after one electron gain is not stable. The Sn−C bond dissociation energy for this species is predicted to be only 0.4 eV by density functional theory (DFT) calculation (B3LYP functional, Def2TZVP//LANL2DZ basis sets), much smaller than for the neutral molecule (predicted 2.3 eV, experimental for organotin compounds ∼2.5 eV).[45]

While very LEEs can decompose TinOH via electron attachment, electrons with higher kinetic energies can promote other mechanisms. Electrons that can transfer >5 eV can bring the tin cage molecules to their electronically excited states, and, at energies >7 eV, they can cause their ionization.[9] Both electronically excited and ionized tin cages undergo facile Sn−C bond cleavage.[8] This is because the lowest unoccupied molecular orbital in the neutral molecule (singly occupied in the ground state of the radical anion) has Sn−C σ^* antibonding character. In the case of ionization, an electron is removed from the highest occupied molecular orbital, which can be described as an Sn−C σ bonding orbital.[31] Thus, in all three cases, the Sn−C bond is significantly weakened.

Electrons with landing energies above the ionization energy are expected to generate SEs in the bulk of the material. Yet, the SE yield induced by incident electrons of different kinetic energies, as well as the energy distribution of those SE, is not known for TinOH (and most other materials). The fact that the densification observed for the whole E_{land} range of 4−36 eV is rather similar (Figure 3a) while the SE emission coefficient in EELS increases is intriguing. We speculate that this phenomenon might be related to similar mean free paths/penetration depths of the incident electrons in this energy range. The conversion of the full thickness into an insoluble material is evidenced by the fact that the exposed areas remain after development. Yet, the exposure to LEEs might lead to a gradient of the film chemical conversion from top to bottom as a result of the short mean free paths of the incident electrons.[46] Unfortunately, the penetration depths/mean free paths of electrons in such low energy range in a complex material such as TinOH are not known and cannot be determined with the present experiments. Therefore, the exact reason for the lack of energy dependence in the compression in the studied E_{land} range remains uncertain.

From the exposed area (30 μm^2) and the difference between the initial thickness of **A** (20 nm) and the thickness of unreacted **A** (as calculated in Figure 5a), we calculated the volume of converted **A** over dose. Together with the film density (from the crystal structure, 1.84 g/cm^3),[27] the TinOH molecular weight (2468.5 g/mol), and electron dose, we can then calculate the number of electrons needed per molecule in average to induce a solubility change as a function of electron energy (Figure 5b). Initially, less than 10 electrons per molecule are required regardless of the energy in the 2−23.6 eV range. This number is in agreement with the number of SE involved in the solubility switch of the material when EUV photons are used, as estimated from previous works in the literature. From the EUV photon dose to render a 40 nm TinOH layer insoluble (D_{100} = 50 mJ/cm^2)[29] mentioned above, it can be estimated that an average of 0.6 EUV photons are absorbed per molecule to yield the insoluble product **B**. Moreover, although an experimental value for total electron yield per absorbed photon in TinOH has not been reported, for a very similar resist material photoelectron emission experiments indicated a yield of 2.3 SE per absorbed EUV photon,[20] whereas a theoretical model proposed 8 SE generated per absorbed photon.[21] The combination of these estimations suggests that an average of 1.4 to 4.8 electrons per molecule could yield the insoluble network, which is within the range of our results.

Similarly, by dividing the reacted volume by the number of electrons, an average reacted volume per incident electron can be estimated (Figure 5b). The maximum obtained reaction volume per electron is 0.15 nm^3. However, this number is only a lower bound because the full film is converted already for the lowest doses studied in the present work.

CONCLUSIONS

Exposure experiments with a LEE microscope on Sn-based EUV resists, tin-oxo cages, allowed us to study the energy and doses of LEEs that are required to render a solubility switch in this material. In situ EELS proved essential to accurately determine the landing energy of the incident electrons on these resist layers. Ex situ AFM analysis of the exposed samples before and after a development process shows that electron exposure yields an insoluble material denser than the original resist and prolonged exposure leads to further densification. This behavior is in agreement with sequential reactions induced by electron irradiation that we simplify as an **A** → **B** → **C** reaction model, resulting from carbon loss and cross-linking of the SnOx inorganic fragments. Thus, **B** represents an insoluble mixture of units cross-linked in low degree, and **C** represents the subsequent formation of a more densified network. Remarkably, electrons with energies as low as 1.2 eV can induce noticeable chemical changes in the resists. Furthermore, it was estimated that fewer than 10 electrons of 2−38 eV per molecule are necessary to render the solubility switch, which corresponds to an average reaction volume of 0.15 nm^3 per electron. The present work uses an unprecedented approach to evidence how crucial electrons of very low energy are essential for the solubility switch of EUV resists, even in low amounts. The insights gained in this investigation are of great value to the understanding of how inorganic EUV resists operate in lithographic applications.

EXPERIMENTAL SECTION

Deposition of the EUV Photoresist. 6.5 × 6.5 mm^2 piranha base-cleaned boron-doped Si substrates (p-type) are used for the preparation of photoresist thin films. The TinOH material[28,29,47] is dissolved in toluene (7.5 mg/mL). Solutions were filtered (0.25 μm polytetrafluoroethylene) right before spin coating. TinOH thin films were obtained by spin coating (acceleration 750 rpm/s, spinning speed 2000 rpm, spinning time 45 s). The thickness of the resulting films was 20 nm, as determined by AFM.

LEE Microscopy. All LEEM/EELS experiments and exposures of photoresist to LEEs were performed using the aberration-corrected ESCHER LEEM experimental setup (Leiden University) based on a commercial LEEM SPECS P90 instrument design. Details about the LEEM outline and the microscope capabilities can be found elsewhere.[33,34,36]

The microscope was operated at an electron gun energy of 15 keV. The emitted 15 keV electrons are slowed down to 0−40 eV energy (E_0) by negative biasing of the sample relative to the grounded objective lens. Specularly reflected and SEs are extracted by this bias field and leave the sample with no possibility of return.

Electron Landing Energy Measurement. Measurements of E_{land} were performed in LEEM using EELS by recording the energy

https://dx.doi.org/10.1021/acsami.9b19004
ACS Appl. Mater. Interfaces XXXX, XXX, XXX−XXX

distribution of electrons emitted and/or reflected from the sample upon exposure of the surface to a primary electron beam of well-defined energy E_0 and current density (I_0). Upon interaction of the primary electron beam with the photoresist surface, depending on the E_0 value, specularly reflected and/or SEs with energy E_{land} leave the sample surface. After passing the electron optics system, beam separators and electron mirror, the reflected and/or SE beam reach the detector and the resulting image, representing an electron energy distribution spectrum in (E, k_y) space (see the Supporting Information) is recorded using a microchannel plate array and a CCD camera. All electron energy distribution spectra are corrected for detector-induced artifacts by subtracting a dark count image, and their intensity is normalized before further analysis.

Exposure to LEEs in LEEM. Exposure to electrons of well-controlled energy, current density, and dose was performed using a beam blanking system. For each single exposure, a value of E_0 is chosen in the 0−40 eV range. The E_0 value was constant during each single exposure. When the exposure was finished, the beam was blanked and the sample was moved to a new unexposed position. The procedure was repeated for each different value of E_0. This approach created a 2D array of exposed areas where one coordinate corresponds to change of dose at constant E_0, while the orthogonal axis corresponds to changes of E_0 at constant dose. After electron exposure in LEEM and AFM analysis of the as-exposed sample, this same sample is developed in 1:3 heptanone/water solution for 30 s. The quality of the resulting patterns is checked using an optical microscope.

Atomic Force Microscopy. The analysis of the sample topography directly after exposure and after development was performed using a commercial AFM instrument (Bruker). The microscope is operated in tapping mode. AFM micrographs are generated using commercial silicon and silicon nitride tips. Analysis of AFM micrographs is performed using Gwyddion software.[48]

DFT Calculations. A model of TinOH was built starting from the crystal structure.[27] The isopropanol molecules were replaced by water molecules to reduce the computational cost. The geometry of the complex was optimized using the B3LYP hybrid functional with the LANL2DZ effective core potential basis set using the Gaussian 16 program.[49] The relatively small basis set was chosen in order to keep the size of the calculations manageable, but we also found that the structures obtained are in better agreement with experimental crystal structures than those optimized using the larger Def2SVP basis set. For better evaluation of the relative energies, we used single point calculations with the Def2TZVP basis set (B3LYP/Def2TZVP//LANL2DZ). Bond dissociation energies were corrected for the differences in zero point vibrational energies (B3LYP/LANL2DZ).

■ ASSOCIATED CONTENT

Supporting Information

The Supporting Information is available free of charge at https://pubs.acs.org/doi/10.1021/acsami.9b19004.

Change of photoresist conductance and SEE coefficient with exposure; compression of the TinOH resist upon exposure; and quantum chemical calculations (PDF)

■ AUTHOR INFORMATION

Corresponding Authors

Ivan Bespalov − *Advanced Research Center for Nanolithography, 1098XG Amsterdam, The Netherlands*; Email: i.bespalov@arcnl.nl

Johannes Jobst − *Kamerlingh Onnes Laboratory, Leiden University, 2333 CA Leiden, The Netherlands*; Email: jobst@physics.leidenuniv.nl

Sonia Castellanos − *Advanced Research Center for Nanolithography, 1098XG Amsterdam, The Netherlands*; orcid.org/0000-0002-4880-1910; Email: s.castellanos@arcnl.nl

Authors

Yu Zhang − *Advanced Research Center for Nanolithography, 1098XG Amsterdam, The Netherlands*

Jarich Haitjema − *Advanced Research Center for Nanolithography, 1098XG Amsterdam, The Netherlands*

Rudolf M. Tromp − *Kamerlingh Onnes Laboratory, Leiden University, 2333 CA Leiden, The Netherlands; IBM T. J. Watson Research Center, Yorktown Heights 10598, New York, United States*

Sense Jan van der Molen − *Kamerlingh Onnes Laboratory, Leiden University, 2333 CA Leiden, The Netherlands*

Albert M. Brouwer − *Advanced Research Center for Nanolithography, 1098XG Amsterdam, The Netherlands; van't Hoff Institute for Molecular Sciences, University of Amsterdam, 1090 GD Amsterdam, The Netherlands*; orcid.org/0000-0002-1731-3869

Complete contact information is available at: https://pubs.acs.org/10.1021/acsami.9b19004

Notes

The authors declare no competing financial interest.

■ ACKNOWLEDGMENTS

Part of this work has been carried out within ARCNL, a public−private partnership between UvA, VU, NWO, and ASML and was partly financed by "Toeslag voor Topconsortia voor Kennis en Innovatie (TKI)" from the Dutch Ministry of Economic Affairs. The authors are grateful to Marcel Hesselberth and Douwe Scholma for their indispensable technical support. The authors also thank Joost Frenken (ARCNL) for insightful discussions and suggestions.

■ REFERENCES

(1) Robinson, A.; Lawson, R. Materials and Processes for Next Generation Lithography. In *Frontiers of Nanoscience*; Palmer, R. E., Ed.; Elsevier, 2016.

(2) Hasan, R. M. M.; Luo, X. Promising Lithography Techniques for Next-Generation Logic Devices. *Nanomanuf. Metrol.* **2018**, *1*, 67−81.

(3) Fallica, R.; Stowers, J. K.; Grenville, A.; Frommhold, A.; Robinson, A. P. G.; Ekinci, Y. Dynamic Absorption Coefficients of Chemically Amplified Resists and Nonchemically Amplified Resists at Extreme Ultraviolet. *J. Micro/Nanolithogr., MEMS, MOEMS* **2016**, *15*, 033506.

(4) Naulleau, P. EUV Lithography Patterning Challenges. In *Frontiers of Nanoscience—Materials and Processes for Next Generation Lithography*; Elsevier Ltd., 2016; Vol. *11*, pp 177−192.

(5) Li, L.; Liu, X.; Pal, S.; Wang, S.; Ober, C. K.; Giannelis, E. P. Extreme Ultraviolet Resist Materials for Sub-7 nm Patterning. *Chem. Soc. Rev.* **2017**, *46*, 4855−4866.

(6) Ashby, P. D.; Olynick, D. L.; Ogletree, D. F.; Naulleau, P. P. Resist Materials for Extreme Ultraviolet Lithography: Toward Low-Cost Single-Digit-Nanometer Patterning. *Adv. Mater.* **2015**, *27*, 5813−5819.

(7) De Simone, D.; Mao, M.; Lazzarino, F.; Vandenberghe, G. Metal Containing Resist Readiness for HVM EUV Lithography. *J. Photopolym. Sci. Technol.* **2016**, *29*, 501−507.

(8) Zhang, Y.; Haitjema, J.; Liu, X.; Johansson, F.; Lindblad, A.; Castellanos, S.; Ottosson, N.; Brouwer, A. M. Photochemical Conversion of Tin-Oxo Cage Compounds Studied Using Hard X-Ray Photoelectron Spectroscopy. *J. Micro/Nanolithogr., MEMS, MOEMS* **2017**, *16*, 023510.

(9) Haitjema, J.; Wu, L.; Giuliani, A.; Nahon, L.; Castellanos, S.; Brouwer, A. M. Photo-Induced Fragmentation of a Tin-Oxo Cage Compound. *J. Photopolym. Sci. Technol.* **2018**, *31*, 243−247.

(10) Cardineau, B.; Del Re, R.; Marnell, M.; Al-Mashat, H.; Vockenhuber, M.; Ekinci, Y.; Sarma, C.; Freedman, D. A.; Brainard, R. L. Photolithographic Properties of Tin-Oxo Clusters Using Extreme Ultraviolet Light (13.5nm). *Microelectron. Eng.* **2014**, *127*, 44−50.
(11) Kostko, O.; Xu, B.; Ahmed, M.; Slaughter, D. S.; Ogletree, D. F.; Closser, K. D.; Prendergast, D. G.; Naulleau, P.; Olynick, D. L.; Ashby, P. D.; et al. Fundamental Understanding of Chemical Processes in Extreme Ultraviolet Resist Materials. *J. Chem. Phys.* **2018**, *149*, 154305.
(12) Fallica, R.; Rezvani, S. J.; Borisov, S.; Simone, D. De; Babin, S.; Lorusso, G.; Vandenberghe, G. The Hidden Energy Tail of Low Energy Electrons in EUV Lithography. *Proc. SPIE* **2019**, *10960*, 1096009.
(13) Thorman, R. M.; Kumar T P, R.; Fairbrother, D. H.; Ingólfsson, O. The Role of Low-Energy Electrons in Focused Electron Beam Induced Deposition: Four Case Studies of Representative Precursors. *Beilstein J. Nanotechnol.* **2015**, *6*, 1904−1926.
(14) Böhler, E.; Warneke, J.; Swiderek, P. Control of Chemical Reactions and Synthesis by Low-Energy Electrons. *Chem. Soc. Rev.* **2013**, *42*, 9219−9231.
(15) Thete, A.; Geelen, D.; Wuister, S.; van der Molen, S. J.; Tromp, R. M. Low-Energy Electron (0-100eV) Interaction with Resists Using LEEM. *Proc. SPIE* **2015**, *9422*, 94220A.
(16) Vaglio Pret, A.; Graves, T.; Blankenship, D.; Biafore, J. J. Modeling and Simulation of Low-Energy Electron Scattering in Organic and Inorganic EUV Photoresists. *Proc. SPIE* **2017**, *10146*, 1014609.
(17) Pollentier, I.; Vesters, Y.; Petersen, J. S.; Vanelderen, P.; Rathore, A.; De Simone, D.; Vandenberghe, G. Unraveling the Role of Secondary Electrons upon Their Interaction with Photoresist during EUV Exposure. *Proc. SPIE* **2017**, *10450*, 104500H.
(18) van Dorp, W. F. Theory: Electron-Induced Chemistry. *Frontiers of Nanoscience—Materials and Processes for Next Generation Lithography*; Elsevier, 2016; Vol. *11*, pp 115−133.
(19) Torok, J.; Re, R. D.; Herbol, H.; Das, S.; Bocharova, I.; Paolucci, A.; Ocola, L. E.; Ventrice, C., Jr.; Lifshin, E. Secondary Electrons in EUV Lithography. *J. Photopolym. Sci. Technol.* **2013**, *26*, 625−634.
(20) Pret, A. V.; Kocsis, M.; De Simone, D.; Vandenberghe, G.; Stowers, J.; Giglia, A.; De Schepper, P.; Mani, A.; Biafore, J. J. Characterizing and Modeling Electrical Response to Light for Metal-Based EUV Photoresists. *Proc. SPIE* **2016**, *9779*, 977906.
(21) Hinsberg, W. D.; Meyers, S. A Numeric Model for the Imaging Mechanism of Metal Oxide EUV Resists. *Proc. SPIE* **2017**, *10146*, 1014604.
(22) Grzeskowiak, S.; Kaminsky, J.; Gibbons, S.; Murphy, M.; Chandonait, J.; Brainard, R. L.; Denbeaux, G. Polymer Effects on PAG Acid Yield in EUV Resists. *Proc. SPIE* **2018**, *10586*, 105860D.
(23) Grzeskowiak, S.; Gibbons, S.; Narasimhan, A.; Brainard, R. L.; Denbeaux, G. Electron Trapping: A Mechanism for Acid Production in Extreme Ultraviolet Photoresists. *J. Micro/Nanolithogr., MEMS, MOEMS* **2018**, *17*, 033501.
(24) Grzeskowiak, S.; Gibbons, S.; Chandonait, J.; Welling, U.; Melvin, L. S.; Kandel, Y.; Brainard, R. L.; Denbeaux, G. Investigating the Threshold Electron Energy for Reactions in EUV Resist Materials. *Proc. SPIE* **2018**, *10586*, 105861N.
(25) Maas, R.; van Lare, M.-C.; Rispens, G.; Wuister, S. F. Stochastics in Extreme Ultraviolet Lithography: Investigating the Role of Microscopic Resist Properties for Metal-Oxide-Based Resists. *J. Micro/Nanolithogr., MEMS, MOEMS* **2018**, *17*, 041003.
(26) Geelen, D.; Jobst, J.; Krasovskii, E. E.; van der Molen, S. J.; Tromp, R. M. Nonuniversal Transverse Electron Mean Free Path Through Few-Layer Graphene. *Phys. Rev. Lett.* **2019**, *123*, 086802.
(27) Banse, F.; Ribot, F.; Toledano, P.; Maquet, J.; Sanchez, C. Hydrolysis of Monobutyltin Trialkoxides: Synthesis and Characterizations of $\{(BuSn)_{12}O_{14}(OH)_6\}(OH)_2$. *Inorg. Chem.* **1995**, *34*, 6371−6379.
(28) Eychenne-Baron, C.; Ribot, F.; Sanchez, C. New Synthesis of the Nanobuilding Block $\{(BuSn)_{12}O_{14}(OH)_6\}^{2+}$ and Exchange Properties of $\{(BuSn)_{12}O_{14}(OH)_6\}(O_3SC_6H_4CH_3)_2$. *J. Organomet. Chem.* **1998**, *567*, 137−142.
(29) Haitjema, J.; Zhang, Y.; Vockenhuber, M.; Kazazis, D.; Ekinci, Y.; Brouwer, A. M. Extreme Ultraviolet Patterning of Tin-Oxo Cages. *J. Micro/Nanolithogr., MEMS, MOEMS* **2017**, *16*, 033510.
(30) Zhang, Y.; Haitjema, J.; Baljozovic, M.; Vockenhuber, M.; Kazazis, D.; Jung, T. A.; Ekinci, Y.; Brouwer, A. M. Dual-Tone Application of a Tin-Oxo Cage Photoresist Under E-Beam and EUV Exposure. *J. Photopolym. Sci. Technol.* **2018**, *31*, 249−255.
(31) Haitjema, J.; Zhang, Y.; Ottosson, N.; Brouwer, A. M. Photoreactions of Tin Oxo Cages, Model EUV Photoresists. *J. Photopolym. Sci. Technol.* **2017**, *30*, 99−102.
(32) Narasimhan, A.; Grzeskowiak, S.; Srivats, B.; Herbol, H. C.; Wisehart, L.; Kelly, C.; Earley, W.; Ocola, L. E.; Neisser, M.; Denbeaux, G.; Brainard, R. L. Studying Secondary Electron Behavior in EUV Resists Using Experimentation and Modeling. *Proc. SPIE* **2015**, *9422*, 942208.
(33) Tromp, R. M.; Hannon, J. B.; Ellis, A. W.; Wan, W.; Berghaus, A.; Schaff, O. A New Aberration-Corrected, Energy-Filtered LEEM/PEEM Instrument. I. Principles and Design. *Ultramicroscopy* **2010**, *110*, 852−861.
(34) Tromp, R. M.; Hannon, J. B.; Wan, W.; Berghaus, A.; Schaff, O. A New Aberration-Corrected, Energy-Filtered LEEM/PEEM Instrument II. Operation and Results. *Ultramicroscopy* **2013**, *127*, 25−39.
(35) Thete, A.; Geelen, D.; van der Molen, S. J.; Tromp, R. M. Charge Catastrophe and Dielectric Breakdown During Exposure of Organic Thin Films to Low-Energy Electron Radiation. *Phys. Rev. Lett.* **2017**, *119*, 266803.
(36) Tromp, R. M.; Fujikawa, Y.; Hannon, J. B.; Ellis, A. W.; Berghaus, A.; Schaff, O. A Simple Energy Filter for Low Energy Electron Microscopy/Photoelectron Emission Microscopy Instruments. *J. Phys.: Condens. Matter* **2009**, *21*, 314007.
(37) Naaman, R.; Sanche, L. Low-Energy Electron Transmission through Thin-Film Molecular and Biomolecular Solids. *Chem. Rev.* **2007**, *107*, 1553−1579.
(38) Frederick, R. T.; Diulus, J. T.; Hutchison, D. C.; Nyman, M.; Herman, G. S. Effect of Oxygen on Thermal and Radiation-Induced Chemistries in a Model Organotin Photoresist. *ACS Appl. Mater. Interfaces* **2019**, *11*, 4514−4522.
(39) Mack, C. A. Development of Positive Photoresists. *J. Electrochem. Soc.* **1987**, *134*, 148−152.
(40) Okoroanyanwu, U. Theory of the Lithographic Process. *Molecular Theory of Lithography*; SPIE: Bellingham, 2015; pp 31−122.
(41) Fallica, R.; Haitjema, J.; Wu, L.; Castellanos, S.; Brouwer, A. M.; Ekinci, Y. Absorption Coefficient of Metal-Containing Photoresists in the Extreme Ultraviolet. *J. Micro/Nanolithogr., MEMS, MOEMS* **2018**, *17*, 023505.
(42) Engmann, S.; Stano, M.; Matejčík, Š.; Ingólfsson, O. Gas Phase Low Energy Electron Induced Decomposition of the Focused Electron Beam Induced Deposition (FEBID) Precursor Trimethyl-(Methylcyclopentadienyl) Platinum(IV) ($MeCpPtMe_3$). *Phys. Chem. Chem. Phys.* **2012**, *14*, 14611−14618.
(43) Wnorowski, K.; Stano, M.; Barszczewska, W.; Jówko, A.; Matejčík, Š. Electron Ionization of $W(CO)_6$: Appearance Energies. *Int. J. Mass Spectrom.* **2012**, *314*, 42−48.
(44) Engmann, S.; Stano, M.; Matejčík, Š.; Ingólfsson, O. The Role of Dissociative Electron Attachment in Focused Electron Beam Induced Processing: A Case Study on Cobalt Tricarbonyl Nitrosyl. *Angew. Chem., Int. Ed.* **2011**, *50*, 9475−9477.
(45) Dean, J. A. Properties of Atoms, Radicals and Bonds. *Lange's Handbook of Chemistry*; McGraw-Hill, Inc., 1999; pp 4.41−4.53.
(46) Torok, J.; Srivats, B.; Memon, S.; Herbol, H.; Schad, J.; Das, S.; Ocola, L.; Denbeaux, G.; Brainard, R. L. Electron Penetration Depths in EUV Photoresists. *J. Photopolym. Sci. Technol.* **2014**, *27*, 611−615.
(47) Van Lokeren, L.; Willem, R.; van der Beek, D.; Davidson, P.; Morris, G. A. Probing the Anions Mediated Associative Behavior of Tin-12 Oxo-Macrocations by Pulsed Field Gradient NMR Spectroscopy. *J. Phys. Chem. C* **2010**, *114*, 16087−16091.

https://dx.doi.org/10.1021/acsami.9b19004
ACS Appl. Mater. Interfaces XXXX, XXX, XXX−XXX

(48) Nečas, D.; Klapetek, P. Gwyddion: An Open-Source Software for SPM Data Analysis. *Cent. Eur. J. Phys.* **2012**, *10*, 181−188.
(49) Frisch, M. J.; Trucks, G. W.; Schlegel, H. B.; Scuseria, G. E.; Robb, M. A.; Cheeseman, J. R.; Scalmani, G.; Barone, V.; Petersson, G. A.; Nakatsuji, H.; Li, X.; Caricato, M.; Marenich, A. V.; Bloino, J.; Janesko, B. G.; Gomperts, R.; Mennucci, B.; Hratch, D. J.; et al. *Gaussian 16*, Revision C.01; Gaussian, Inc.: Wallingford CT, 2016.

https://dx.doi.org/10.1021/acsami.9b19004
ACS Appl. Mater. Interfaces XXXX, XXX, XXX−XXX